ELSEVIER

Journal of Fluids and Structures 23 (2007) 479–499

JOURNAL OF FLUIDS AND STRUCTURES

www.elsevier.com/locate/jfs

A systematic approach to the numerical calculation of fundamental quantities of the two-dimensional flow over a circular cylinder

O. Posdziech[a,*], R. Grundmann[b]

[a]*EBZ Entwicklungs- und Vertriebsgesellschaft Brennstoffzelle mbH, Görlitzer Str. 28, D-01099 Dresden, Germany*
[b]*Institute of Aerospace Engineering, Dresden University of Technology, D-01062 Dresden, Germany*

Received 18 October 2005; accepted 27 September 2006
Available online 28 November 2006

Abstract

The flow around an infinitely long circular cylinder at Reynolds numbers between $5 \leqslant Re \leqslant 250$ is investigated numerically by means of a spectral element method. Careful studies of the effect of resolution and extension of the computational domain on drag and lift forces, base-pressure coefficient and Strouhal number are performed in the laminar, two-dimensional regime. Asymptotic results are obtained by increasing the size of the computational domain to several thousands of cylinder diameters. It is shown that, in contrast to the Strouhal number, the force coefficients and the base-pressure coefficient are strongly dependent on the resolution and even more on the size of the computational domain. For both the asymptotic and finite domains, the Reynolds number relationships are compared to numerical and experimental data from the literature. The results accurately reproduce experimental findings and explain deviations of former numerical investigations. Our database is useful both for validation of numerical codes and measurement verifications where the separation of physical features and effects of experimental arrangements are frequently an open question.

Keywords: Circular cylinder; Two-dimensional flow; Asymptotic solution

1. Introduction

The flow around an unconfined circular cylinder of infinite length is a classical problem of fluid dynamics. Despite the simple geometry, the cylinder flow shows many phenomena in a relatively small range of Reynolds numbers that also occur in more complex cases. Examples are flow separation, the primary instability with development of the unsteady von Kármán vortex street, transition to three-dimensionality with interaction of 'mode A' and 'mode B' instabilities, the occurrence of turbulence in the wake, and the Kelvin–Helmholtz instability of the separated shear layer. The cylinder flow has been investigated for more than one century, starting with fundamental work of Strouhal (1878) on the dependency between frequency of vortex shedding, free-stream velocity, and cylinder diameter. Other experiments, including those by Wieselsberger (1921), Roshko (1954), Tritton (1959), and Berger (1964), revealed qualitative and quantitative features of

*Corresponding author.
E-mail address: oliver.posdziech@ebz-dresden.de (O. Posdziech).

0889-9746/$ - see front matter
doi:10.1016/j.jfluidstructs.2006.09.004

the flow at low Reynolds numbers. Numerical investigations, starting from steady and two-dimensional, aimed at validating the measured results. Extensive reviews can be found in Braza et al. (1986) and Lange (1997).

A strong revival of interest on flow around a cylinder could be noted at the end of last century in the form of extensive experimental and numerical investigations. In particular, better experimental techniques allowed a deeper insight into the structure of the cylinder wake. Influences from the cylinder ends, length-to-diameter ratio, free-stream turbulence, blockage, vibrations, and three-dimensional effects were identified to cause the large scatter in earlier experimental results (Gerich and Eckelmann, 1982; Williamson, 1989, 1992; Norberg, 1994).

Numerical works were first targeted at steady cylinder flows to calculate the drag, pressure and velocity (resp. vorticity) distributions, as well as the separation lengths. Later, with the expansion to unsteady simulations, time-dependent quantities including the Strouhal number were determined. Mostly, only a few selected Reynolds numbers were investigated. Extensive studies on resolution as well as blockage effects, i.e. the ratio of domain extension and cylinder diameter, were not carried out, since computer capacity was strongly limited in the past. The main interest was frequently a validation and demonstration of new computer codes and techniques and not the accurate computation of flow quantities. From that, the large scatter in the available database can be explained.

Examples for analyzes of the influence of computational domain extensions on the drag at low Reynolds numbers can be found in Fornberg (1980), Behr et al. (1995), Anagnostopoulos et al. (1996), Lange (1997), and Kravchenko et al. (1999). Fornberg ($\mathrm{Re} = 20$), Behr et al. ($\mathrm{Re} = 100$), Anagnostopoulos et al. ($\mathrm{Re} = 106$) as well as Kravchenko et al. ($\mathrm{Re} = 100$) concentrated on one Reynolds number, whereas Lange investigated the flow around a circular cylinder at very low Reynolds numbers ($\mathrm{Re} < 10$). On the other hand, Rosenfeld (1994) and Yang et al. (1994) varied the number of grid points but retained a fixed size domain. Persillon and Braza (1998) varied, both the number of grid points and the domain extension; however, this was accomplished simultaneously.

Numerous experimental as well as numerical works dealt with the Reynolds number dependency of flow quantities like the base-pressure coefficient and the Strouhal number. Newer examples on the experimental side can be found in Williamson (1989, 1992) or Norberg (1994). On the numerical side, Reynolds number dependencies of the Strouhal number and the base-pressure coefficient, that can easily be used to compare with experimental results, are computed together with the drag and lift forces that cannot be measured accurately. Examples can be found in Franke et al. (1990) and Yang et al. (1994), where only steady results were given. Henderson (1995) published two-dimensional results for the variation of drag components and the base-pressure coefficient with Reynolds number in the form of curve-fits. However, because of the small domain extension, results are not grid independent. A similar work was published by Park et al. (1998), where the flow quantities at Reynolds numbers between 2 and 160 are given. Blockage effects are diminished compared to the work of Henderson because of a larger domain extension. Since the domain-independence has been investigated by looking at the Strouhal number in most numerical works, considerable errors can result in flow quantities like lift, drag, and especially the base-pressure coefficient, because the Strouhal number is least effected by the domain size (see Section 4).

In this paper, two-dimensional numerical simulations of the flow around a circular cylinder at Reynolds numbers between 5 and 250 using a spectral element method are presented. Details of the code are shown in Section 2. One of the qualities of this global discretization scheme is the simplicity of grid refinement, e.g. improvement of resolution, by increasing the order of polynomial basis within the spectral elements. Resolution as well as extension of the computational domain are varied systematically and separately to receive domain-independent flow quantities. Because the independence from the domain extension seems to be an arbitrary assumption of the different authors, asymptotic solutions were searched by using extremely large domain sizes. This was accomplished for the steady regime as shown in Section 3, as well as for the unsteady cylinder flow in Section 4. The effect of domain extension is shown for the drag, base-pressure coefficient, lift, and Strouhal number (the two last-mentioned only in the unsteady case). The domain dependency of flow quantities is given as polynomial approximations and compared to data from literature.

Finally, two sizes of the computational domain are used to determine the Reynolds number relationship of the flow quantities in the steady and unsteady regime, as shown in Section 5. The results of the present work are compared to experimental as well numerical data. In Section 6 the Strouhal–Reynolds number relationship is investigated. For it, a new formulation of curve fitting is proposed and compared to traditional polynomial approximations.

2. Numerical procedure

We consider Newtonian, incompressible, and time-dependent flows with constant properties governed by the Navier–Stokes equations written in nondimensional form,

$$\frac{\partial \boldsymbol{u}}{\partial t} + \boldsymbol{N}(\boldsymbol{u}) = \nabla p + \frac{1}{\mathrm{Re}} \nabla^2 \boldsymbol{u} \quad \text{in } \Omega, \tag{1}$$

$$\nabla \cdot \boldsymbol{u} = 0 \quad \text{in } \Omega, \tag{2}$$

where $\boldsymbol{u}(x, y, t)$ is the velocity field and $p(x, y, t)$ the pressure field, and t is the nondimensional time. The variables are nondimensionalized by the free-stream velocity U_∞ and the cylinder diameter D. The Reynolds number Re is defined as $\mathrm{Re} = U_\infty D/\nu$ with ν the kinematic viscosity. The term $\boldsymbol{N}(\boldsymbol{u})$ in Eq. (1) represents the nonlinear advection operator, here used in rotational form

$$\boldsymbol{N}(\boldsymbol{u}) = \frac{1}{2}\nabla(\boldsymbol{u} \cdot \boldsymbol{u}) - \boldsymbol{u} \times \nabla \times \boldsymbol{u}. \tag{3}$$

Time discretization is performed by means of a three-step splitting scheme of order J, with J up to third order introduced in Karniadakis et al. (1991), where the nonlinear terms are computed explicitly, while the pressure and viscous corrections are treated implicitly. The two-dimensional domain (x, y) is partitioned into K spectral elements. Within each element, a high-order polynomial basis represents the solution as well as the geometry. This basis can be constructed as a product of one-dimensional Gauss–Lobatto–Legendre polynomials to form the discrete solution. Thus, the two-dimensional field is described by KN^2 numbers, where N is the number of basis coefficients or polynomial order in each direction. Besides the fast convergence and high accuracy of global spectral methods, intensive use is made of the simplicity of grid refinement by increasing the order of polynomial basis. Further details of the code can be found in Henderson and Karniadakis (1995).

Although a physically unconfined cylinder is considered, the discretized equations require finite boundaries in the far-field. First, some fundamental length definitions are introduced to characterize the extension of domain boundaries that are responsible for the ubiquitous blockage effects. The definition of inflow length, distance of upper/lower boundaries and output length are shown in Fig. 1. The calculations have been performed on a mesh with a semicircular inflow boundary. So, the inflow length L_i and length of upper/lower boundary L_b are equal. The blockage ratio $H/D = 2L_b/D$ is frequently used to characterize the effects of domain extensions, neglecting the action of a finite inflow length in rectangular domains. We will use the definitions L_i/D, L_b/D, L_o/D throughout this work.

Fig. 2 shows a mesh with $K = 186$ spectral elements and an order of polynomial basis with $N = 4$. The number of elements and its location around the cylinder surface were tested intensively. Results from calculations with a very large number of elements and low order of polynomial basis were compared to those with few elements and large polynomial orders. We did not observe quantitative differences, but a mesh with a medium number of elements was chosen for computational efficiency reasons. The outflow length was set to a constant value of $L_o = 50D$ after tests in the unsteady flow regime, in order to avoid an effect of unphysical reflections from the outflow boundary on the solution. The inflow length L_i resp. the length of the upper/lower boundary L_b were varied in the present work between $L_{b|i} = 20D$ and $L_{b|i} = 4000D$. For $L_{b|i} = 20D, 40D, 70D$ and $120D$, a mesh with $K = 186$ spectral elements was chosen. The inner mesh remained constant, whereas the boundary location was expanded. In the case of higher domain extensions, additional elements are grouped around the outer boundary. Therefore, the number of spectral elements was $K = 246$, 306, and 396 for $L_{b|i} = 500D$, $2000D$, and $4000D$, respectively. A computational time step of $\delta t = 0.005$ was used in all

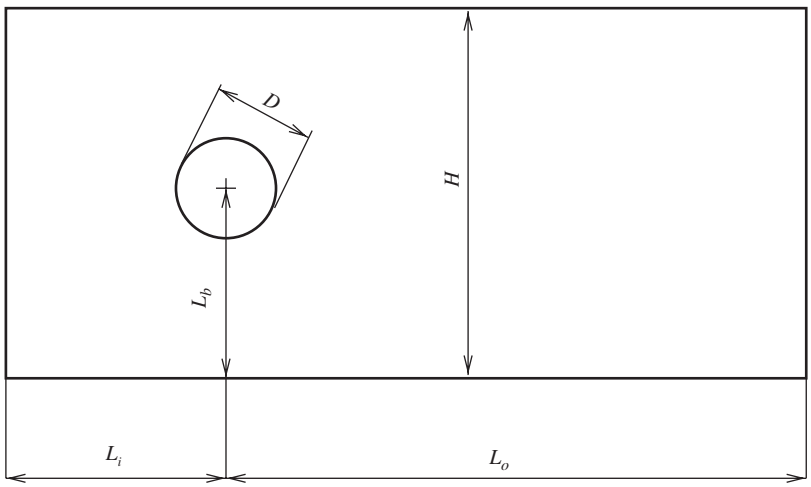

Fig. 1. Definition of domain extensions.

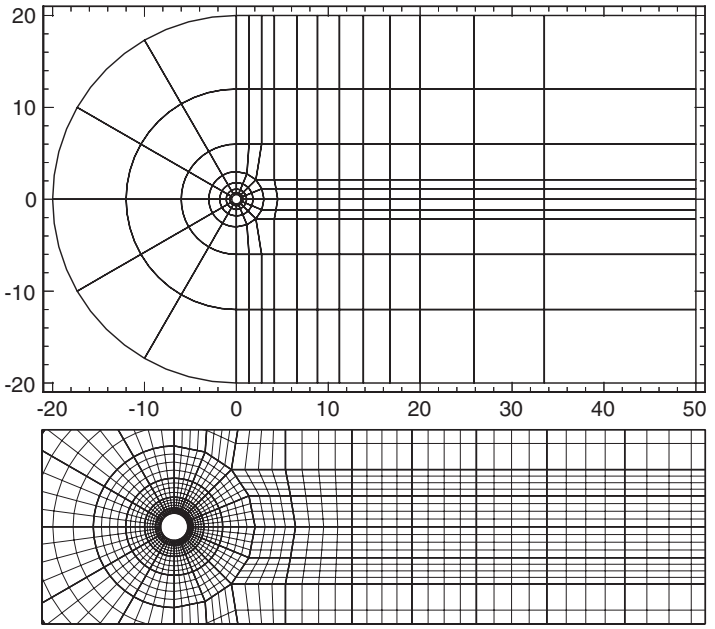

Fig. 2. Spectral elements (above) and mesh near the cylinder (below) for $N = 4$ as used in this study: $L_{b|i} = 20D$, $L_o = 50D$.

computations. Doubling the time step did not change the results. The small step size was chosen because of stability requirements at higher Reynolds numbers.

Boundary conditions are the no-slip condition ($u = 0$, $v = 0$) at the surface of the cylinder and outflow ($(\boldsymbol{n} \cdot \nabla)\boldsymbol{u} = 0$) downstream from the cylinder. The pressure is set to zero at the outflow boundary, along the other boundaries a high-order pressure condition of Neumann type is used to control divergence errors introduced by the splitting scheme (Karniadakis et al., 1991). Free stream ($u = 1$, $v = 0$) is applied to the inflow, top, and bottom boundaries. These boundary conditions are critical to blockage effects. Some type of asymptotic boundary conditions (Fornberg, 1980; Dennis, 1976) would guarantee a satisfying solution for finite boundaries located closer to the cylinder surface. Since highly sophisticated boundary conditions are difficult to implement and to recommend to similar investigations, we restrict our study to the simpler free-stream boundary condition. Tests with a potential flow solution as boundary condition showed that the solution is only remarkably influenced if the blockage is very high (Anagnostopoulos et al., 1996). The potential flow solution is not accurate enough to result in a proper reflection of cylinder flow. If the inflow and upper/lower boundary lengths are large, the potential flow solution passes into the free-stream values.

Boundary conditions seem to have a minor significance in order to prevent blockage effects. The mixture of Dirichlet and von Neumann boundary conditions $\partial u/\partial y = 0$, $v = 0$ at upper/lower domain boundaries used in Persillon and Braza (1998) was not able to lessen blockage compared to the simple free-stream condition applied in this study.

The accuracy of numerical results is compared by means of integral quantities like drag and lift forces, the base-pressure coefficient and the Strouhal number. The forces on a cylinder are defined as follows:

$$\boldsymbol{F}(t) = \oint (-p\boldsymbol{n} + \nu(\nabla\boldsymbol{u} + \nabla\boldsymbol{u}^{\top}) \cdot \boldsymbol{n})\,\mathrm{d}s. \tag{4}$$

Using the free-stream velocity U_∞, density ρ, and the diameter D, drag and lift coefficients are written as

$$C_D = \frac{F_D}{(1/2)\rho U_\infty^2 D}, \quad C_L = \frac{F_L}{(1/2)\rho U_\infty^2 D}. \tag{5}$$

A frequently considered quantity is the nondimensional pressure at the rear stagnation point, called 'base-pressure' or 'base-suction' coefficient $-C_{p_b}$. The base-pressure coefficient is easier to measure than forces in the low Reynolds number regime as considered here, so it is used to compare measurements and numerics. Generally, the base-pressure coefficient is defined as

$$C_{p_b} = \frac{P - P_\infty}{(1/2)\rho U_\infty^2}, \tag{6}$$

where in the case of an unsteady flow regime ($\mathrm{Re}>47$) the mean value has to be used. Experimentalists measure the pressure at the rear stagnation point and the inflow conditions to get the base-pressure coefficient. The determination from simulations is less straightforward. The free-stream velocity U_∞ is given as boundary condition and the pressure at the rear stagnation point is read from the data field, but a correct definition of P_∞ is difficult. Different forms to involve the reference pressure are used in the literature. Henderson (1995) and most other authors use the pressure at the inflow boundary P_{inlet}, whereas Braza et al. (1986) the pressure at the front stagnation point P_0. The latter definition is probably used in Persillon and Braza (1998). Both definitions are strongly dependent on blockage effects, because the pressure at the inlet as well as at the front stagnation point adjusts to the distance of the inlet boundary. Therefore, two sources of deviations exist for the base-pressure coefficient in small computational domains.

The most frequently used flow quantity is the nondimensional frequency of vortex shedding in the unsteady flow regime, defined by

$$\mathrm{St}=\frac{fD}{U_\infty}. \tag{7}$$

The vortex shedding frequency f can be measured easily compared to forces or pressures.

Numerous curve-fits are given in the paper in order to quantify the dependency of flow quantities from the domain extension or from the Reynolds number. The accuracy of curve-fits is estimated by means of the mean deviation $\overline{\varepsilon}$ and maximum deviation $\varepsilon_{\max}$ as defined by

$$\overline{\varepsilon}=\frac{1}{N}\sum_{i=1}^{N}|C_{\mathrm{calc}}-C_{\mathrm{fit}}|, \tag{8}$$

$$\varepsilon_{\max}=|C_{\mathrm{calc}}-C_{\mathrm{fit}}|_{\max}. \tag{9}$$

The general coefficient C stands for drag, lift, base-pressure coefficients, and Strouhal number, as the case may be.

3. Asymptotic solution in the steady regime

In order to find an asymptotic solution for the flow around an infinitely long circular cylinder, the computational domain was extended stepwise from $L_{b|i}=20D$ up to $L_{b|i}=4000D$ as described in Section 2. The resolution was improved by increasing the polynomial order from $N=6$ to 14. Since the domain size and the resolution were varied independently, it could be studied how both quantities affect the flow parameters. In the steady regime ($\mathrm{Re}<47$), three Reynolds numbers ($\mathrm{Re}=5,20,40$) were investigated closer to check grid independence of the solution.

The procedure of establishing grid independence will be made clear with the example of $\mathrm{Re}=20$. Fig. 3 (inset) shows how the drag coefficient changes with the order of polynomial basis if the domain size is hold fixed. The different curves correspond to the domain extension of $L_{b|i}=20D$–$4000D$. It can be seen easily that the drag remains constant for $N\geqslant 10$ at all domain extensions. Furthermore, the influence of the resolution is weaker than the errors that result from the blockage effect. However, the spectral elements are strongly tightened near the cylinder wall, so results are accurate even if a low polynomial order is used.

After the proof that the drag is independent on the number of grid points, the dependency of the drag coefficient on the domain extension was investigated as shown in Fig. 3 (large view). It should be noted that the domain size is plotted in logarithmic scale. It is aimed to find an asymptotic or at least close to asymptotic solution. The drag coefficient grows exponentially with decreasing domain size. If the domain extension is increased to $L_{b|i}\geqslant 1000D$, the solution can be considered as being grid independent. Deviations of the drag between $L_{b|i}=2000D$ and $4000D$ are below 0.1%, therefore we claim to have reached an asymptotic solution. The drag coefficient from the present work is compared to a selection of numerical data from literature, as shown in Fig. 3. The locations of the outer boundaries of the different studies are given in Table 1.

Experimental data are not included because it is not possible to measure very low forces accurately. Although different boundary conditions have been used in the far-field, the data of Fornberg (1980), Henderson (1995), Lange (1997) and Yang et al. (1994) fit accurately to the curve from the present work. This supports the presumption that the boundary condition has a minor influence compared to the domain extension. Only the drag coefficient obtained in Park et al. (1998) is lower than expected. The small domain extension in the wake of the cylinder ($L_o=20D$) could be the cause of the deviation. Fornberg performed an investigation at $\mathrm{Re}=20$ concerning the maximal vorticity for different boundary conditions in the far-field with varied domain extensions. Although only two different grids were

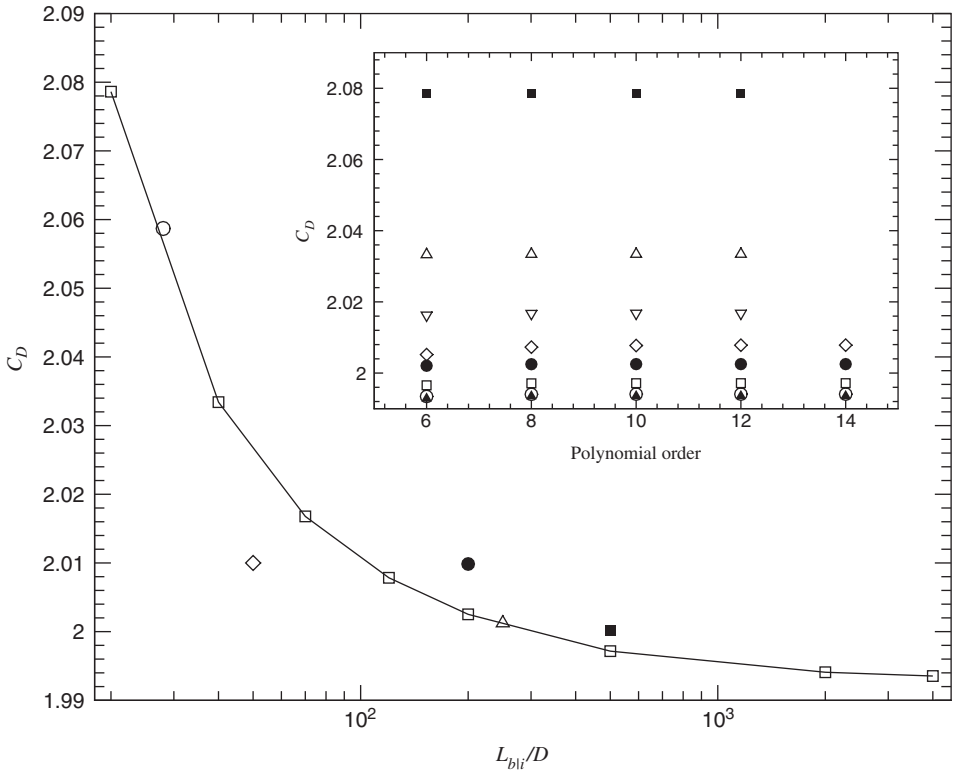

Fig. 3. Drag coefficient versus domain extension $L_{b|i}$ and order of polynomial basis at Re = 20. Large figure: ■, Fornberg (1980); ○, Henderson (1995); Δ, Lange (1997); ◇, Park et al. (1998); ●, Yang et al. (1994); □, present work. Inset: ■, $L_{b|i} = 20D$; △, $40D$; ▽, $70D$; ◇, $120D$; ●, $200D$; □, $500D$; ○, $2000D$; ◇, $4000D$.

Table 1
Comparison of domain extensions as used in different numerical works

	L_i/D	L_b/D	L_o/D
Behr et al. (1995)	8	4.5–16	22.5
Franke et al. (1990)	20	20	20
Henderson (1995)	16	28	25
Kravchenko et al. (1999)	10–60	10–60	10–60
Lange (1997)	30	30	130
Park et al. (1998)	50	50	20
Persillon and Braza (1998)	9.85	8.23	>17
Rosenfeld (1994)	30.5	30.5	30.5
Yang et al. (1994)	200	200	200
Present work	20–4000	20–4000	50

used to check the resolution, the drag coefficient of $C_D = 2.0001 \pm 0.0001$ perfectly reflects the result of the present study as shown in Fig. 3. Lange studied the effect of domain extension on the drag at very low Reynolds numbers in detail, so that the correspondence is excellent. The work of Henderson focused on the Reynolds number dependency of the drag. Because a rather small rectangular mesh was used (see Table 1), the resulting drag is too high and deviates slightly from our curve which was generated under the assumption of a semicircular inflow domain. The data of Yang et al. were generated in order to verify a new numerical concept. Nevertheless, the domain size and number of grid points were chosen carefully, so that result corresponds accurately to the curve in Fig. 3. A good compromise between accuracy and effort is made if the outer boundaries are located within the largest curvature of the C_D versus

$L_{b|i}$ curve from Fig. 3. The error in the drag coefficient is lower or equal 1% if an extension of $L_{b|i} \geqslant 70D$ is used, as shown in Table 2.

The drag coefficients in dependency on the domain extension are further given in Fig. 4 for Re = 5, 20 and 40. The domain size is again plotted in logarithmic scale. At Re = 5 the deviation between the drag at $L_{b|i} = 20D$ and $4000D$ is about 7%. The diagrams at Re = 20 and 40 are scaled with the 7% error as lower limit of the y-axis. The blockage effect is increased with decreasing Reynolds number in the steady flow regime as was also shown in Lange (1997). With the exception of Re = 5, the drag remains nearly constant for $L_{b|i} \geqslant 1000D$.

The frictional, pressure, total drag, and the base-pressure coefficients for the different domain extensions are summarized in Table 2. Deviations from the asymptotic values (e_{C_D}, $e_{-C_{p_b}}$), taken from the data at $L_{b|i} = 4000D$, are also given in the table. It can be seen again that at Re = 5 and $L_{b|i} = 20D$ the error of the drag coefficient amounts to about 7% compared to 3.6% at Re = 40. The situation is even worse if the base-pressure coefficient is considered. The blockage effect increases the base-pressure by 18% at Re = 5 and $L_{b|i} = 20D$. At Re = 40 the error still amounts to about 13.5%. As already stated in Section 2, a large error occurs since both the pressure at the rear stagnation point and the reference pressure are strongly governed by the blockage effect.

The comparison between different numerical results in Fig. 3 showed that the data match accurately the curve of the present work. Therefore, a polynomial expression of the drag and base-pressure coefficients is given that can be used to estimate errors caused by blockage effects due to finite domain extensions. The exponential decrease of drag with increasing location of the outer boundaries $L_{b|i}/D$ is favorably approximated by polynomials with noninteger exponents as defined in Eq. (10).

$$C = a_0 + a_1(L_{b|i}/D)^{-a_2}. \tag{10}$$

The coefficient C stands for the drag and the base-pressure respectively. Table 3 gives the coefficients of drag and base-pressure approximations. The coefficient a_0 can be used as asymptotic value for very large sizes of the computational

Table 2
Drag and base-pressure versus domain extension in the steady regime

$L_{b\|i}/D$	C_{D_p}	C_{D_f}	C_D	$-C_{p_b}$	$e_{C_D}/(\%)$	$e_{-C_{p_b}}/(\%)$
Re = 5						
20	2.2396	1.9507	4.1904	1.0878	7.17	18.02
40	2.1595	1.8872	4.0467	1.0022	3.50	8.73
70	2.1300	1.8600	3.9915	0.9693	2.09	5.17
120	2.1113	1.8488	3.9601	0.9483	1.28	2.88
200	2.1013	1.8407	3.9420	0.9405	0.82	2.04
500	2.0907	1.8322	3.9229	0.9293	0.33	0.82
2000	2.0846	1.8273	3.9118	0.9229	0.05	0.12
4000	2.0834	1.8264	3.9099	0.9217	0	0
Re = 20						
20	1.2552	0.8234	2.0786	0.6188	4.27	14.82
40	1.2259	0.8075	2.0334	0.5765	2.00	6.97
70	1.2151	0.8017	2.0168	0.5609	1.17	4.07
120	1.2093	0.7985	2.0078	0.5524	0.72	2.49
200	1.2059	0.7966	2.0025	0.5475	0.45	1.58
500	1.2024	0.7947	1.9972	0.5424	0.18	0.64
2000	1.2004	0.7936	1.9941	0.5395	0.03	0.10
4000	1.2001	0.7935	1.9935	0.5389	0	0
Re = 40						
20	1.0167	0.5317	1.5484	0.5373	3.63	13.47
40	0.9956	0.5230	1.5187	0.5025	1.64	6.12
70	0.9850	0.5200	1.5081	0.4901	0.68	3.48
120	0.9843	0.5183	1.5027	0.4830	0.56	1.99
200	0.9821	0.5174	1.4995	0.4799	0.35	1.33
500	0.9798	0.5165	1.4963	0.4761	0.14	0.53
2000	0.9786	0.5160	1.4945	0.4739	0.02	0.08
4000	0.9784	0.5159	1.4942	0.4736	0	0

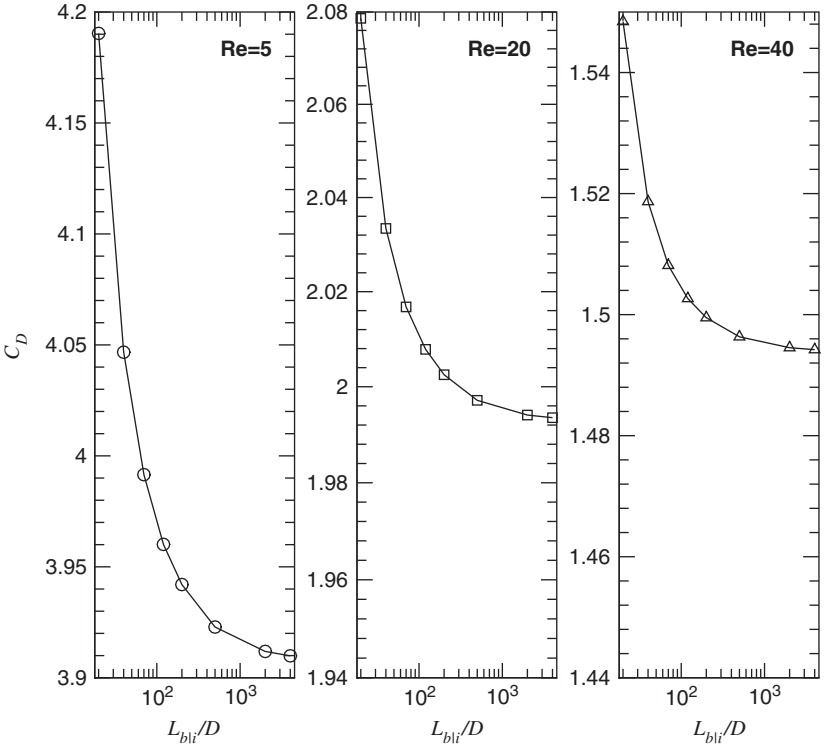

Fig. 4. Drag coefficients versus extension of computational domain for different Reynolds numbers in the steady regime: ○, Re = 5; □, Re = 20; △, Re = 40 (error about 7%, respectively).

Table 3
Polynomial approximation of drag and base-pressure coefficients in the steady regime

	Re = 5	Re = 20	Re = 40
C_D			
a_0	3.906566	1.993045	1.493902
a_1	4.593203	1.583433	1.493902
a_2	0.929342	0.974151	1.021031
$\overline{\varepsilon}$	0.00242	0.00071	0.00051
$\varepsilon_{\max}$	0.00887	0.00318	0.00210
$-C_{p_b}$			
a_0	0.920229	0.538523	0.474423
a_1	2.761453	1.407086	1.907100
a_2	0.935271	0.960673	1.133408
$\overline{\varepsilon}$	0.00177	0.00077	0.00062
$\varepsilon_{\max}$	0.0057	0.0027	0.0010

domain. The mean and maximal deviations ($\overline{\varepsilon}$ and $\varepsilon_{\max}$) between the computed datapoints and the curve-fit are included as defined in Eqs. (8) and (9), respectively.

4. Asymptotic solution in the unsteady regime

If the Reynolds number exceeds 47, the flow behind a circular cylinder becomes unsteady and a von Kármán vortex street develops. Computation in this flow regime are more laborious to establish the unsteady flow field. Domain

extensions $L_{b|i}$ from $20D$ to $4000D$ were chosen again to identify the effect of domain size on the integral quantities of the cylinder flow. The Reynolds number was varied from $\mathrm{Re} = 50$ to 250 within this study. It should be noted that the flow becomes three-dimensional for $\mathrm{Re} > 190$, as shown in Posdziech and Grundmann (2001). The simulations were restricted to two dimensions, so that this effect cannot be observed here. The drag and lift coefficients as well as the base-pressure coefficient vary with time because of the unsteady flow regime. Therefore, mean quantities have to be used. More than 50 shedding cycles were computed to establish the flow in all cases and more than 20 cycles for averaging the flow quantities. If the flow is established and the resolution is sufficient, then the flow quantities show a nearly perfect sinusodial behavior for $\mathrm{Re} \leqslant 250$.

The same procedures as in the steady regime were repeated in order to find grid-independent solutions. Since the flow structures in the wake are much more complex in the unsteady regime, a rather high Reynolds number of 200 was chosen to search for the minimal polynomial order. For each domain extension the resolution was improved by increasing the order of polynomial basis from $N = 6$ to 12 for $L_{b|i} \leqslant 120D$ and to $N = 14$ for $L_{b|i} > 120D$, until the mean drag coefficient remained constant as shown in Fig. 5 (inset). An order of polynomial basis of $N = 12$ can be noted as sufficiently resolved at all sizes of the computational domain. The error that results from an unsufficient resolution is small compared to the error that is made if the domain extension is too small, if a polynomial order of at least $N \geqslant 8$ is used. In Fig. 5 (large part) the dependency of the domain extension $L_{b|i}/D$ on the mean drag is given and compared to data from literature. The drag coefficient is taken from simulations with a polynomial order of 12. It should be noted again that the domain extension has been plotted logarithmically. The drag coefficient of Henderson (1995) fits perfectly to the curve of the present work, whereas the drag that is given in Lange (1997) is larger than expected. It is supposed that the resolution was not sufficient for larger Reynolds numbers in his work. Rosenfeld (1994) performed a grid refinement study with an O-type grid at a fixed size of $60D$ and with a strong expansion towards the far-field. The given drag coefficient is slightly smaller than expected, however, the reasons are not clear.

Fig. 6 shows the same two views for the Strouhal number. Both the error from small domain extensions and from an insufficient resolution are much lower compared to those of the drag coefficient. Data given by Henderson (1995), Rosenfeld (1994) and Lange (1997) fit perfectly in the given curve. An interesting feature can be seen in the inset of Fig. 6: if the domain extension is smaller than $100D$, the Strouhal number is underestimated if the resolution is not

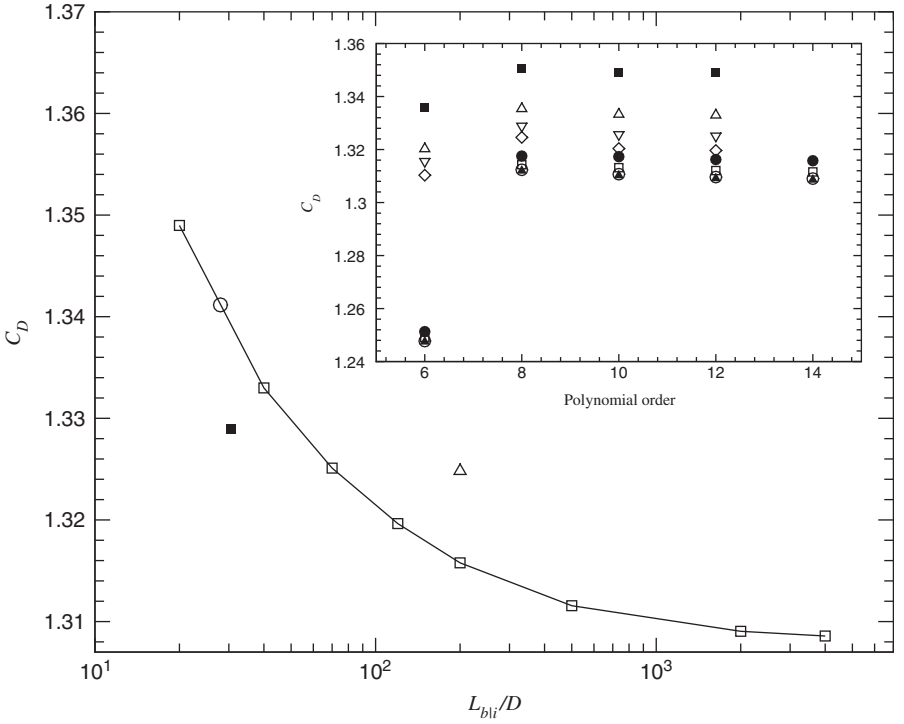

Fig. 5. Mean drag coefficient versus domain extension $L_{b|i}$ and order of polynomial basis at $\mathrm{Re} = 200$: Large figure: ○, Henderson (1995); △, Lange (1997); ■, Rosenfeld (1994); □, present work. Inset: ■, $L_{b|i} = 20D$; △, $40D$; ▽, $70D$; ◇, $120D$; •, $200D$; □, $500D$; ○, $2000D$; ▲, $4000D$.

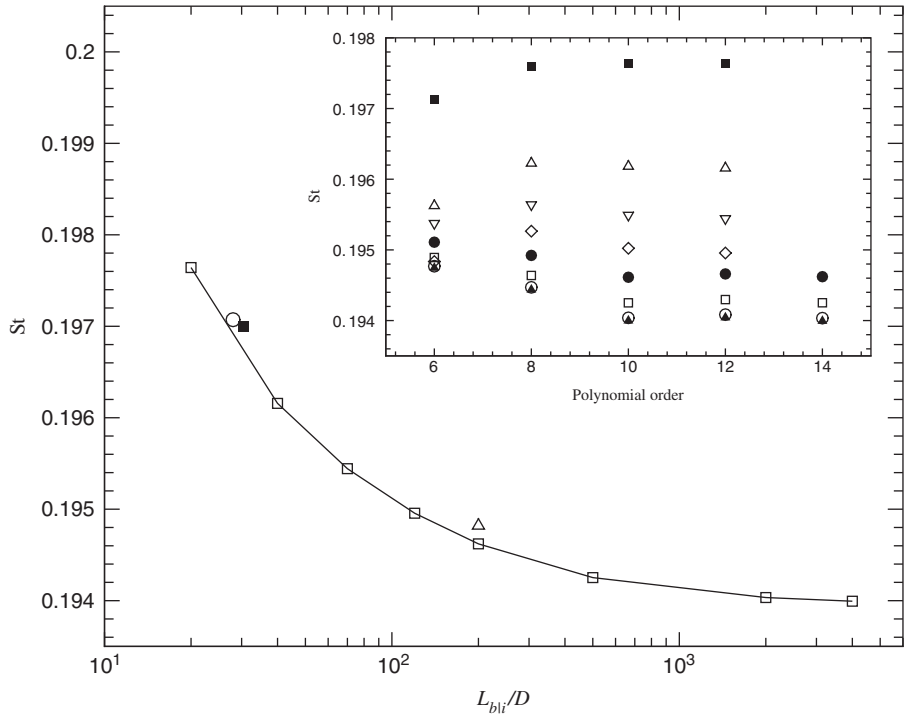

Fig. 6. Strouhal number versus domain extension $L_{b|i}$ and order of polynomial basis at Re = 200. Large figure: ○, Henderson (1995); △, Lange (1997); ■, Rosenfeld (1994); □, present work. Inset: ■, $L_{b|i} = 20D$; △, $40D$; ▽, $70D$; ◇, $120D$; ●, $200D$; □, $500D$; ○, $2000D$; ▲, $4000D$.

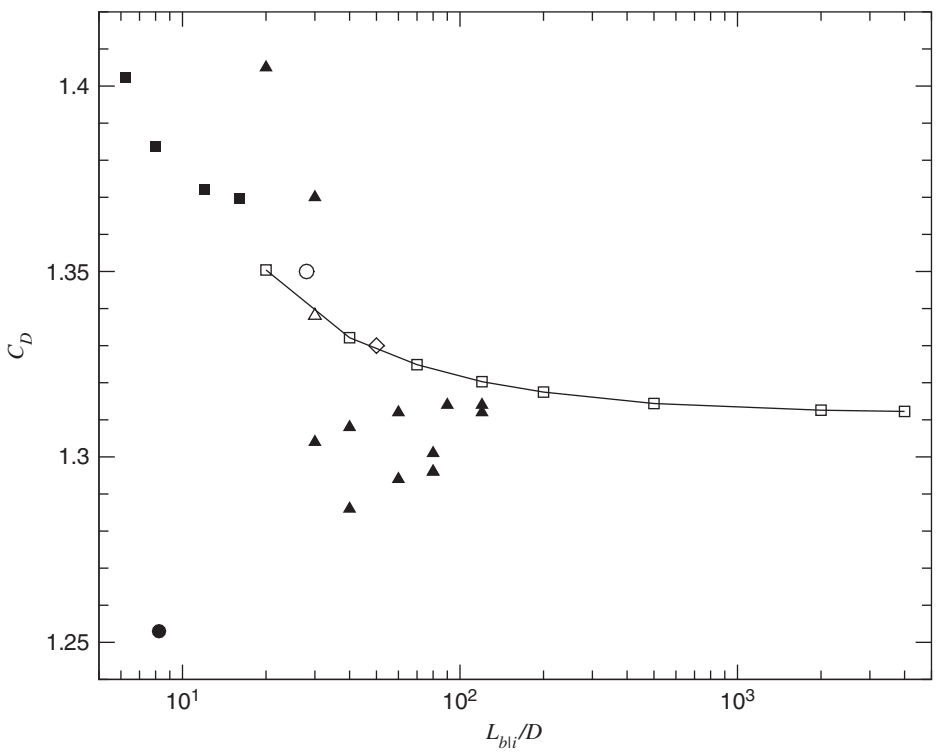

Fig. 7. Mean drag coefficient versus domain extension $L_{b|i}$ at Re = 100: ○, Henderson (1995); △, Lange (1997); ◇, Park et al. (1998); ▲, Kravchenko et al. (1999); ■, Behr et al. (1995); ●, Persillon and Braza (1998); □, present work.

sufficient. The figure exposes why the code validation by means of the Strouhal number is critical. If the Strouhal number is in a certain range of error, the other quantities do not. And even worse, an insufficient resolution can decrease the Strouhal number, whereas small domain extensions increase it. Both effects are able to compensate each other. A comparison of the Strouhal number with data from the literature cannot assure a grid-independent numerical solution. Flow quantities like the drag and the base-pressure coefficients are considerably more influenced by the blockage effect and a poor resolution.

Next, $\mathrm{Re} = 100$ is considered, because a larger set of data can be found in the literature at this Reynolds number. The dependency of the mean drag coefficient on the domain extension is shown in Fig. 7. Kravchenko et al. (1999) performed a code validation study by means of unsteady cylinder data at $\mathrm{Re} = 100$ in order to investigate the effect of the domain size. It can be seen that their drag data are strongly scattered. Therefore, it is supposed that, unlike the present work, a sufficient resolution was not guaranteed simultaneously or the number of shedding cycles that were used to establish the flow was to low (in some cases only 8 shedding cycles compared to 50 in the present work). A larger error can also be observed in the data of Persillon and Braza (1998) where the code validation was performed by means of the Strouhal number. As stated before, it is supposed that a large blockage effect and an insufficient resolution compensate each other. Data of Behr et al. (1995), Park et al. (1998), Lange (1997) and Henderson (1995) fit perfectly to our curve according to the domain extensions that were used.

The characteristic flow quantities (Strouhal number, lift, mean drag, and mean base-pressure coefficients) in dependency on domain extensions at $\mathrm{Re} = 100$ and 200 are summarized in Table 4. Besides that, the percentage deviation from the asymptotic value at $L_{b|i} = 4000D$ is given. It can be seen that the error is rather similar at $\mathrm{Re} = 100$ and 200 for all flow quantities. This stands in contrast to the steady flow regime, where the error is diminished with increasing Reynolds number. It should be noted also that the absolute drag decreases strongly with increasing Reynolds number in the steady regime. The Strouhal number is much less influenced by the blockage effect. If the domain extension exceeds $200D$, then the error is below 1% in all cases. Besides the base-pressure coefficient, the other flow quantities are satisfyingly reflected for domains as small as $L_{b|i} = 70D$. In any case, the use of domains that are smaller than $20D$ has to be avoided.

Analoguously to the steady case, a curve-fit is given for the relationship between flow quantities and the domain extension. Again the polynomial approximation of Eq. (10) is applied. Table 5 lists the coefficients of the polynomial for the drag, lift, Strouhal number, and base-pressure coefficients, together with the mean and maximum deviations as given in Eqs. (8) and (9). It can be seen that the usage of polynomials with noninteger exponents results in a very accurate curve-fit because of the exponential decay of flow quantities with increasing domain extension. Even if the curves are only valid for the semi-circular inflow boundary as used in the present work, data from the literature fit very well to this representation as can be seen in Figs. 5–7.

Table 4
Characteristic flow quantities versus domain extension in the unsteady regime

$L_{b\|i}/D$	St	C_L	C_D	$-C_{p_b}$	$e_{\mathrm{St}}(\%)$	$e_{C_L}(\%)$	$e_{C_D}(\%)$	$e_{-C_{p_b}}(\%)$
$\mathrm{Re} = 100$								
20	0.1667	0.3309	1.3504	0.7448	2.06	4.69	2.91	7.91
40	0.1650	0.3238	1.3321	0.7188	1.05	2.42	1.51	4.15
70	0.1644	0.3210	1.3249	0.7083	0.66	1.56	0.96	2.63
120	0.1640	0.3193	1.3203	0.7014	0.42	1.01	0.61	1.63
200	0.1638	0.3182	1.3175	0.6977	0.27	0.66	0.40	1.09
500	0.1635	0.3170	1.3144	0.6932	0.11	0.27	0.16	0.45
2000	0.1633	0.3162	1.3126	0.6906	0.02	0.04	0.03	0.07
4000	0.1633	0.3161	1.3123	0.6901	0	0	0	0
$\mathrm{Re} = 200$								
20	0.1976	0.6880	1.3490	1.0097	1.88	4.02	3.09	6.83
40	0.1962	0.6781	1.3330	0.9843	1.11	2.53	1.87	4.15
70	0.1954	0.6728	1.3251	0.9717	0.75	1.73	1.26	2.82
120	0.1950	0.6691	1.3196	0.9628	0.50	1.16	0.85	1.88
200	0.1946	0.6664	1.3158	0.9567	0.32	0.76	0.55	1.23
500	0.1943	0.6635	1.3116	0.9499	0.13	0.32	0.23	0.51
2000	0.1940	0.6617	1.3090	0.9458	0.02	0.05	0.04	0.08
4000	0.1940	0.6614	1.3086	0.9451	0	0	0	0

Table 5
Polynomial approximation of flow quantities in the unsteady regime (Eq. (10))

	Re = 50	Re = 100	Re = 150	Re = 200	Re = 250
St					
a_0	0.121691	0.163290	0.182377	0.193909	0.201736
a_1	0.070135	0.047697	0.035103	0.032678	0.028323
a_2	0.971843	0.880607	0.780594	0.724154	0.641835
$\overline{\varepsilon}$	0.000041	0.000023	0.000015	0.000013	0.000034
$\varepsilon_{\max}$	0.00014	0.00010	0.00007	0.00003	0.00008
C_L					
a_0	0.048007	0.315945	0.503038	0.659813	0.786065
a_1	0.118070	0.189247	0.186956	0.182915	0.211279
a_2	0.864397	0.850838	0.740338	0.624851	0.589645
$\overline{\varepsilon}$	0.000090	0.000119	0.000071	0.000147	0.000420
$\varepsilon_{\max}$	0.00030	0.00039	0.00019	0.00052	0.00095
C_D					
a_0	1.401544	1.311982	1.299216	1.307388	1.325016
a_1	0.894291	0.498911	0.368882	0.336582	0.317611
a_2	0.962251	0.857583	0.771942	0.696743	0.663560
$\overline{\varepsilon}$	0.000508	0.000229	0.000249	0.000162	0.000319
$\varepsilon_{\max}$	0.00183	0.00093	0.00062	0.00027	0.00134
$-C_{p_b}$					
a_0	0.489992	0.689934	0.827189	0.941818	1.042474
a_1	1.215210	0.747739	0.573994	0.481216	0.470695
a_2	1.000716	0.872701	0.767476	0.654087	0.606200
$\overline{\varepsilon}$	0.000538	0.000272	0.000194	0.000351	0.000727
$\varepsilon_{\max}$	0.00183	0.00106	0.00090	0.00114	0.00192

A detailed analysis of the effect of resolution (i.e. number of grid points) as well as domain extension was shown in the previous sections. The grid-independence of the numerical solution is assured for Reynolds numbers between 5 and 250 if the domain size exceeds $L_{b|i} > 1000D$. But even for smaller domains, accurate solutions can be obtained if a certain error in the representation of the flow quantities is accepted. It was further shown that the Strouhal number is the worst choice if grid independence is verified in numerical simulations. A number of publications suffer from that.

5. Dependency of flow quantities on Reynolds number

In the following, the dependencies of characteristic flow quantities on Reynolds number in the range $10 \leqslant \mathrm{Re} \leqslant 250$ are shown. Drag and base-pressure coefficients versus Reynolds number are provided in the steady flow regime. The mean drag and base-pressure as well as the lift coefficients versus Reynolds number are given in the unsteady case. The Strouhal number will be treated separately (see Section 6) because of the good comparability to experimental data. Results of the present work are included with domain extensions of $L_{b|i} = 70D$, $L_o = 50D$ and $L_{b|i} = 4000D$, $L_o = 50D$. Grids with 186, respectively 396, spectral elements were used. The order of polynomial basis was set to $N = 10$ and 12. The computational domain with $L_{b|i} = 70D$ represents a good compromise between accuracy and economics, whereas the grid with $L_{b|i} = 4000D$ was proven as an asymptotic solution.

Fig. 8 shows the C_D versus Re relationship in the steady regime at Reynolds numbers between 10 and 50. It should be noted that, because of the strong dependency of the drag on Reynolds number under steady flow conditions, the differences between the data-sets seems to be small within the curve diagram. An exception is the work of Henderson (1995), where the drag exceeds that of the present work because of the blockage effect. On the other hand, the drag coefficients that were obtained by Dennis (1976), Lange (1997), Park et al. (1998) and Yang et al. (1994) fit accurately to the data of the present work. All authors used rather large computational domains (see Table 1) compared to other investigations that were published and are not included here because of the large deviations. The inset within Fig. 8

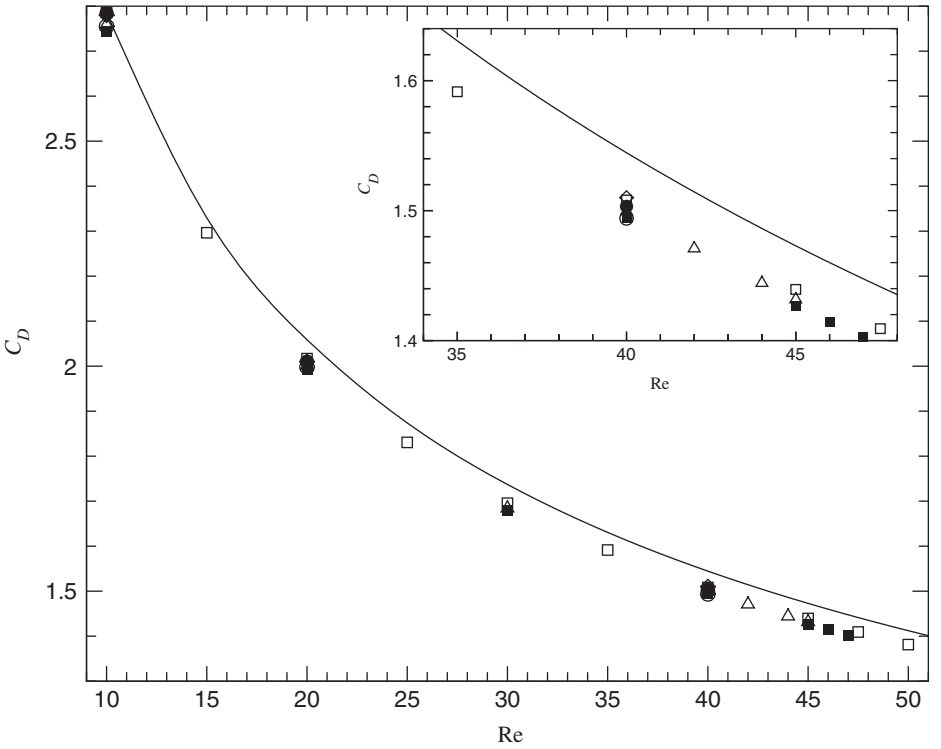

Fig. 8. Drag coefficient versus Reynolds number in the steady flow regime:—, Henderson (1995); ○, Dennis (1976); △, Lange (1997); ◇, Park et al. (1998); •, Yang et al. (1994); □, present work $L_{b|i} = 70D$ ■, present work $L_{b|i} = 4000D$.

zooms in on the Reynolds number dependency of the drag ($35 \leqslant \mathrm{Re} \leqslant 50$). Here differences between results of the present work with $L_{b|i} = 70D$ and $4000D$ as well as to data from the literature can easily be seen. The deviations occur in accordance to the domain sizes that were used. The reader is referred to Section 3 for a closer insight into the dependency of the drag on the domain size.

The base-pressure coefficient is even more strongly dependent on the domain size. Therefore, differences between data of the present work with domain extensions $L_{b|i} = 70D$ and $4000D$ are larger, as shown in Fig. 9. If the results are compared to data of Henderson (1995), a nearly constant displacement of his curve due to the smaller computational domain is noted. Experimental data of Williamson and Roshko (1990) are also included in the figure. However, the measured results are largely scattered at low Reynolds numbers, so that the comparison is only qualitative.

Next, the dependency of the mean drag coefficient on Reynolds number is shown in the unsteady regime at $\mathrm{Re} > 47$. Since the drag variation is smaller compared to the steady case, differences between data from literature and that of the present work are easily identifiable in Fig. 10. Drag coefficients of Henderson (1995), Park et al. (1998), and both sets of the present work are nearly parallel in correspondence with the domain extensions that were used in each case. An exception is the data of Lange (1997) and in particular that of Persillon and Braza (1998). Lange used a domain with $L_{b|i} = 30D$ for his transient calculations, consequently data are slightly higher. The drag at $\mathrm{Re} = 200$ is very close to that of present results, probably because of an insufficient resolution. Apparently the number of grid points that were used by Persillon and Braza was too low to obtain accurate solutions in the unsteady regime. Since they applied a very small domain extension (see Table 1) the drag should be higher. That the grid was probably not fine enough can be seen on the plot of the time-dependent drag coefficient in the two-dimensional regime in their Fig. 8. It should be perfect sinusoidal if the resolution is sufficient.

Unlike the drag, the lift coefficient strongly increases with Reynolds number. As a result, the distance of the von Kármán vortices from the centerline becomes higher and the effect of low domain extensions is strengthened. The lift coefficient versus Reynolds number is shown in Fig. 11. Again, differences between the numerical data are difficult to identify due to the strong change of the lift with increasing Reynolds number. Data of Park et al. (1998) and that of the present work are nearly identical. For $\mathrm{Re} > 170$, the error due to the blockage effect increases as the differences between both data-sets of the present work indicate. The data of Franke et al. (1990) that are included in Fig. 11 show a lower

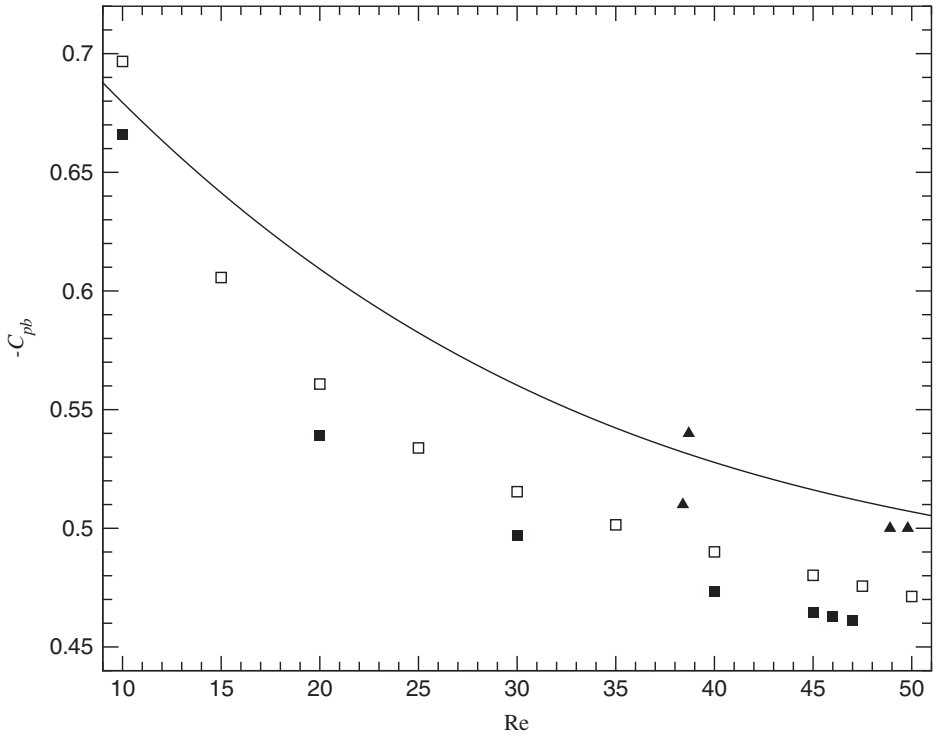

Fig. 9. Base-pressure coefficient versus Reynolds number in the steady flow regime: —, Henderson (1995); ▲, Williamson and Roshko (1990); □, present work $L_{b|i} = 70D$ ■, present work $L_{b|i} = 4000D$.

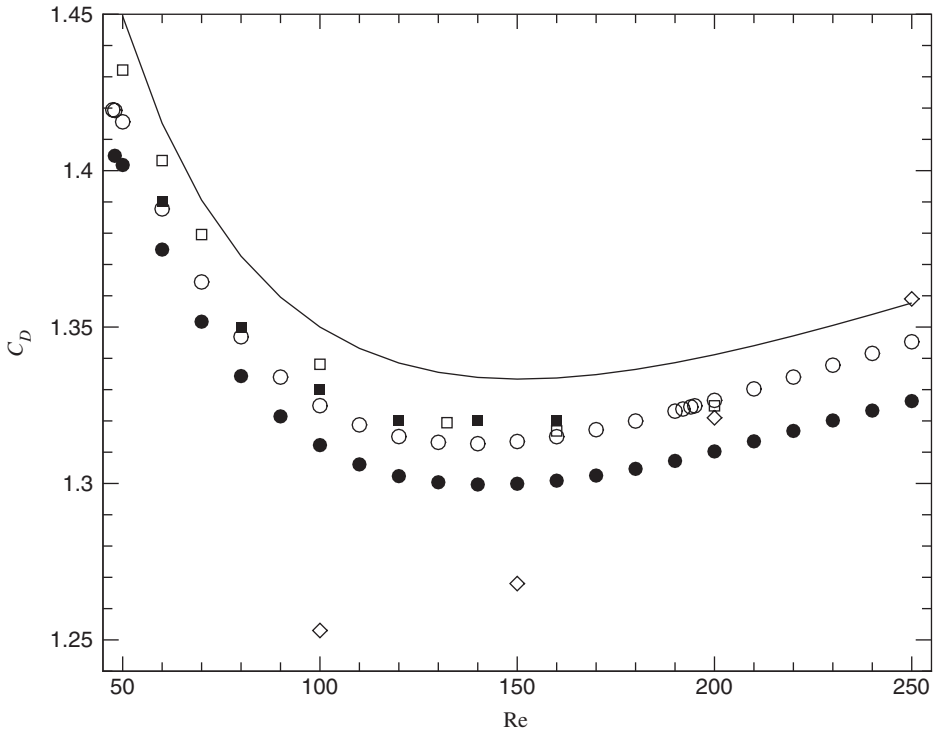

Fig. 10. Mean drag coefficient versus Reynolds number in the unsteady flow regime: —, Henderson (1995); □, Lange (1997); ■, Park et al. (1998); ◇, Persillon and Braza (1998); ○, present work $L_{b|i} = 70D$; •, present work $L_{b|i} = 4000D$.

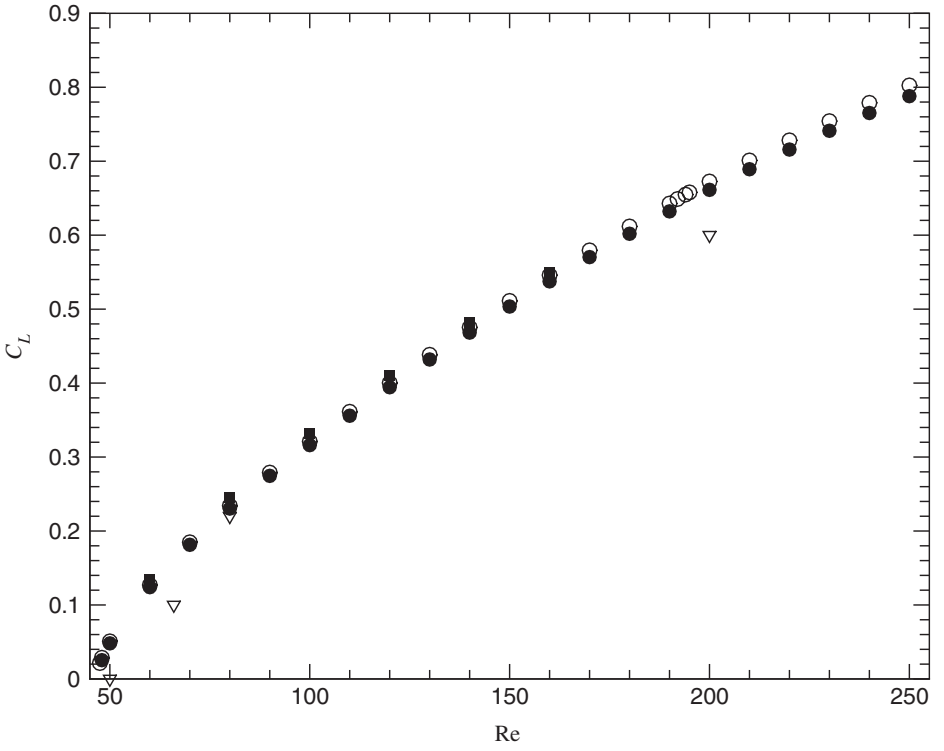

Fig. 11. Lift coefficient versus Reynolds number in the unsteady flow regime: ▽, Franke et al. (1990); ■, Park et al. (1998); ○, present work $L_{b|i} = 70D$; ●, present work $L_{b|i} = 4000D$.

lift coefficient than expected from the domain extension as given in Table 1. An insufficient resolution is mostly the cause of such a deviation.

The Reynolds number dependency of the mean base-pressure coefficient (see Fig. 12) clearly indicates the effect of the domain size. Data of Henderson (1995) and of the present work are nearly parallel. Since the domain extension of Henderson was much smaller (see Table 1) compared to $L_{b|i} = 70D$ and $4000D$ as used in the present work, the data-sets deviate as was already shown in Section 4. The data-point of Persillon and Braza (1998) at $\mathrm{Re} = 100$ is strongly affected by the small computational domain as well as by the definition of base-pressure coefficient that was used in their study. Experimental results of Williamson and Roshko (1990) and Norberg (1994) are included in Fig. 12. The data fit accurately to that of the present work up to a Reynolds number of about 170. At higher Reynolds numbers measurements are governed by the formation of three-dimensional modes in the wake of the circular cylinder (Posdziech and Grundmann, 2001). It should be noted that the experimental data slightly shift to higher base-pressures compared to the numerical results. But it has to be kept in mind that the experimental arrangements are influenced by blockage effects, because of the limitations of the wind or water channels, and by end effects since the cylinder that is used is not infinitely long. Further, the accurate measurement of very low pressures is difficult to perform. Even the size of the boreholes has an effect on the pressure output.

Finally, the Reynolds number dependency of drag, lift, and base-pressure coefficients are given as polynomial approximations. In the case of the steady flow ($\mathrm{Re} < 47$) an approximation with noninteger polynomials as given in Eq. (10) performed best with lowest mean $\bar{\varepsilon}$ (see Eq. (8)) and maximal deviations $\varepsilon_{\max}$ (Eq. (9)) compared to approximations with integer polynomials of different order. The fit is valid for a Reynolds number range of $5 \leqslant \mathrm{Re} \leqslant 50$. The coefficients of the polynomial are summarized in Table 6 for $L_{b|i} = 70D$ as well as $L_{b|i} = 4000D$.

The flow quantities in the unsteady flow regime ($50 \leqslant \mathrm{Re} \leqslant 250$) are approximated successfully by a fifth order polynomial,

$$C = a_0 + a_1 \frac{L_{b|i}}{D} + a_2 \left(\frac{L_{b|i}}{D}\right)^2 + a_3 \left(\frac{L_{b|i}}{D}\right)^3 + a_4 \left(\frac{L_{b|i}}{D}\right)^4 + a_5 \left(\frac{L_{b|i}}{D}\right)^5. \tag{11}$$

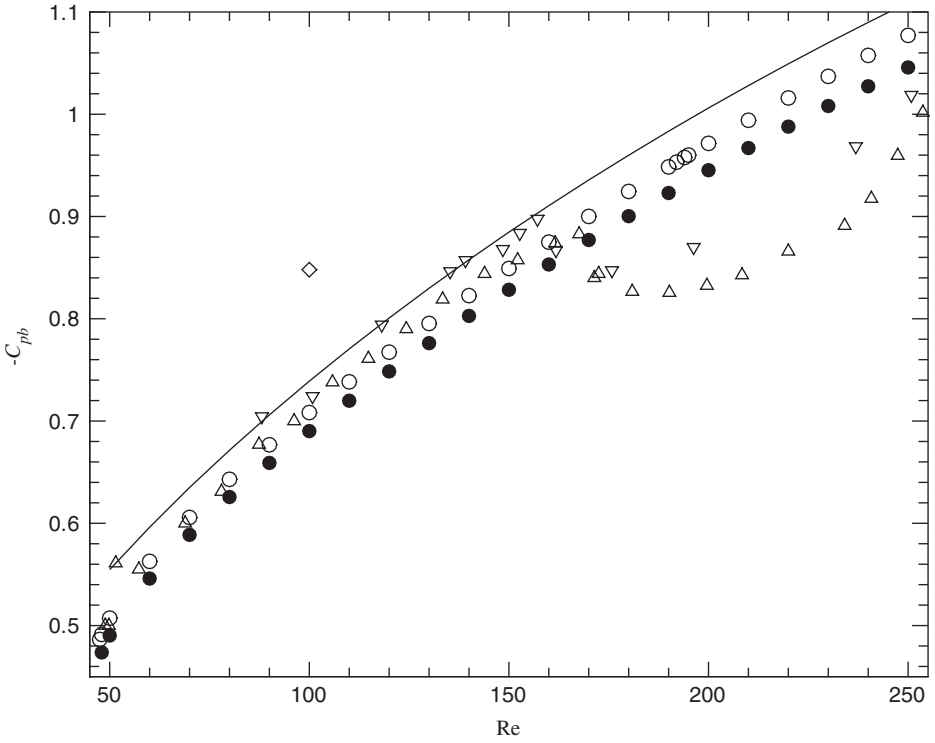

Fig. 12. Mean base-pressure coefficient versus Reynolds in the unsteady flow regime: —, Henderson (1995); ⋄, Persillon and Braza (1998); △, Williamson and Roshko (1990); ▽, Norberg (1994); ○, present work $L_{b|i} = 70D$; •, present work $L_{b|i} = 4000D$.

Table 6
Polynomial approximation of the Reynolds number dependencies in the steady regime (Eq. (10))

	$L_{b\|i} = 70D$		$L_{b\|i} = 4000D$	
	C_D	$-C_{p_b}$	C_D	$-C_{p_b}$
a_0	0.5345136	0.4098829	0.5076150	0.4137402
a_1	9.2441768	2.5526812	8.8648267	2.5915967
a_2	0.6110109	0.9436754	0.5954448	1.0124978
$\overline{\varepsilon}$	0.00326	0.00222	0.00275	0.00220
$\varepsilon_{\max}$	0.01239	0.00836	0.01369	0.00532

The related coefficients are given for both $L_{b|i} = 70D$ and $4000D$ in Table 7. The correspondence of the drag and the base-pressure approximations with the numerical data is excellent, whereas the mean and maximal deviations are slightly higher (in the order of 1×10^{-3}) in the case of the lift coefficient.

If the Reynolds number exceeds a critical value Re_C, the stationary flow, characterized by two symmetrical vortices in the near wake, passes into a time-dependent flow regime and it develops the well-known von Kármán vortex street. This primary instability of the cylinder flow results from a global Hopf bifurcation of the steady flow. A critical Reynolds number $\mathrm{Re}_C = 46.7 \pm 0.1$ has been obtained from the intersection of the steady and transient drag curves. It agrees well with results of a stability analysis by Jackson (1987) giving $\mathrm{Re}_C = 46.184$, as well as experiments by Provansal et al. (1987) where $\mathrm{Re}_C\ (L/D \to \infty) = 47$, Leweke and Provansal (1995) with $\mathrm{Re}_C = 46.8$, and Norberg (1994) as well as Fey (1998) with $\mathrm{Re}_C \approx 47$. The critical Reynolds number of the primary instability can be viewed as exactly reproducible with both experimental and numerical means.

Table 7
Polynomial approximation of the Reynolds number dependencies in the unsteady regime (Eq. (11))

	C_D	C_L	$-C_{p_b}$
$L_{b\|i} = 70D$			
a_0	1.70116	−0.621939	0.0355849
a_1	-8.8129×10^{-3}	2.183×10^{-2}	1.4888×10^{-2}
a_2	7.706×10^{-5}	-2.2733×10^{-4}	-1.4643×10^{-4}
a_3	-3.3247×10^{-7}	1.4224×10^{-6}	8.8359×10^{-7}
a_4	7.369×10^{-10}	-4.402×10^{-9}	-2.6547×10^{-9}
a_5	-6.6816×10^{-13}	5.2702×10^{-12}	3.109×10^{-12}
$\overline{\varepsilon}$	0.00017	0.00100	0.00064
$\varepsilon_{\max}$	0.00085	0.00328	0.00216
$L_{b\|i} = 4000D$			
a_0	1.68474	−0.627192	0.0232106
a_1	-8.7685×10^{-3}	2.1989×10^{-2}	1.4688×10^{-2}
a_2	7.775×10^{-5}	-2.3043×10^{-4}	-1.4304×10^{-4}
a_3	-3.4396×10^{-7}	1.4446×10^{-6}	8.56329×10^{-7}
a_4	7.8551×10^{-10}	-4.4791×10^{-9}	-2.56552×10^{-9}
a_5	-7.3668×10^{-13}	5.3718×10^{-12}	3.00309×10^{-12}
$\overline{\varepsilon}$	0.00024	0.00114	0.000833
$\varepsilon_{\max}$	0.00093	0.00334	0.002374

6. Strouhal–Reynolds number relationship

The determination of the St versus Re relationship at low Reynolds numbers preoccupied experimentalists for more than five decades. Roshko (1954), Tritton (1959), Berger (1964), Williamson (1989), Williamson (1992), Norberg (1994), Leweke and Provansal (1995), Fey (1998) and others published data in the two-dimensional regime up to $\mathrm{Re} \approx 170, \ldots, 180$. Beginning with Williamson's (1989) work, the curves show a nearly perfect agreement if parallel vortex shedding is forced. This has been achieved by a proper choice of measurement conditions, such as the usage of end-plates to avoid oblique vortex shedding, a large cylinder length-to-diameter ratio and a simultaneous suppression of cylinder vibrations. The vortex shedding frequency and with it the Strouhal number can be measured easily and accurately compared to the base-pressure coefficient or the forces that act on the cylinder. In order to enforce parallel vortex shedding, different means are used: Wiliamson, Norberg and Fey used end-plates, whereas Leweke and Provansal measured the vortex shedding frequency on a ring that simulates an infinitely long circular cylinder. The utilization of end-plates carries the risk that the flow quantities are affected by the tilting angle (Posdziech and Grundmann, 2001) so that the experimental results are not independent from the experimental set-up.

On the numerical side, data-sets of the Strouhal–Reynolds number relationship are found in among others Lange (1997) and Henderson (1997). A number of data are given in Persillon and Braza (1998) and therefore included in the present paper. Results of the present work were obtained with domain extensions of $L_{b|i} = 70D$, $L_o = 50D$ and $L_{b|i} = 4000D$, $L_o = 50D$, 186 (respectively 396) spectral elements and an order of polynomial basis of $N = 10$ as well as $N = 12$. The St versus Re relationship in the two-dimensional regime is shown in Fig. 13. Results are compared to experimental and numerical data from literature. Since the curves run closely together, it can be stated that the Strouhal number is exactly reproducible by experimental as well as numerical means. However, it has to be taken into account that the Strouhal number is much less sensitive to errors due to an insufficient resolution or blockage effects, as already pointed out in Section 4. In order to illustrate differences in the results, a segment of Fig. 13 for $100 \leqslant \mathrm{Re} \leqslant 170$ is displayed in Fig. 14. The numerical results that were taken from literature were computed by using smaller domains compared to that of the present work. Therefore, the Strouhal–Reynolds number dependency that was obtained by Henderson (1997) is located consistently above the results of the present work due to a higher blockage. Data of Lange (1997) show the expected progression only at $\mathrm{Re} \leqslant 100$. As already discussed in Section 4, there seems to be an underresolution at higher Reynolds numbers, so that the Strouhal number decreases in comparison to that of the present work. The Strouhal number that was obtained by Persillon and Braza (1998) at $\mathrm{Re} = 100$ fits accurately to the measured data, but stands in contradiction to the used domain size. At $\mathrm{Re} = 150$ the Strouhal number is under- and at $\mathrm{Re} = 200$ overestimated. It has been stated before that the resolution was probably not sufficient for an accurate determination of the Strouhal number.

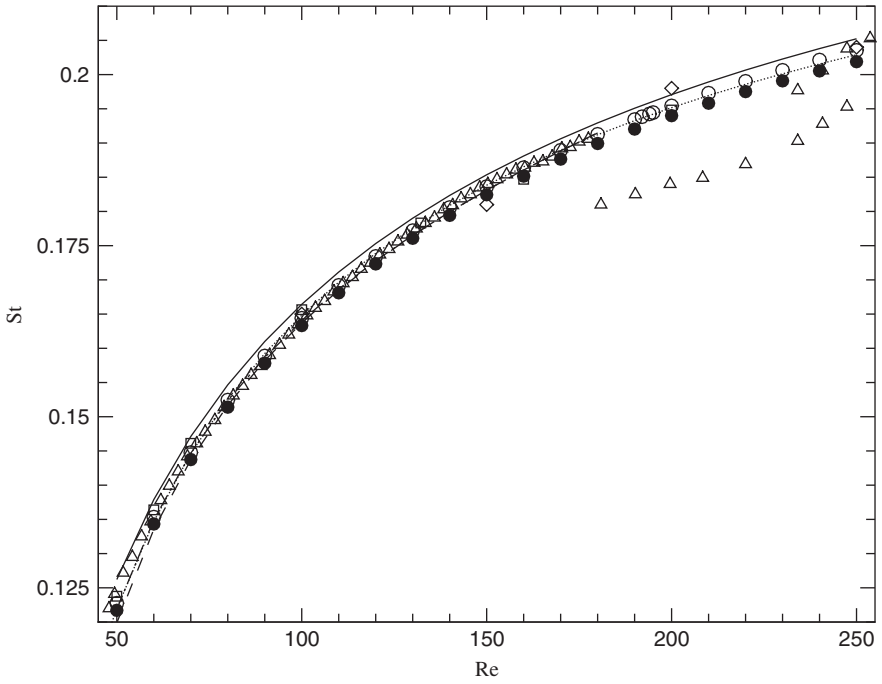

Fig. 13. Strouhal–Reynolds number relationship: —, Henderson (1997); □, Lange (1997); ◇, Persillon and Braza (1998); ○, present work $L_{b|i} = 70D$; •, present work $L_{b|i} = 4000D$ (all numerics); ·····, Fey (1998); – – – – ––, Leweke and Provansal (1995); – · – · –, Norberg (1994); △, Williamson (1989) (all experiments).

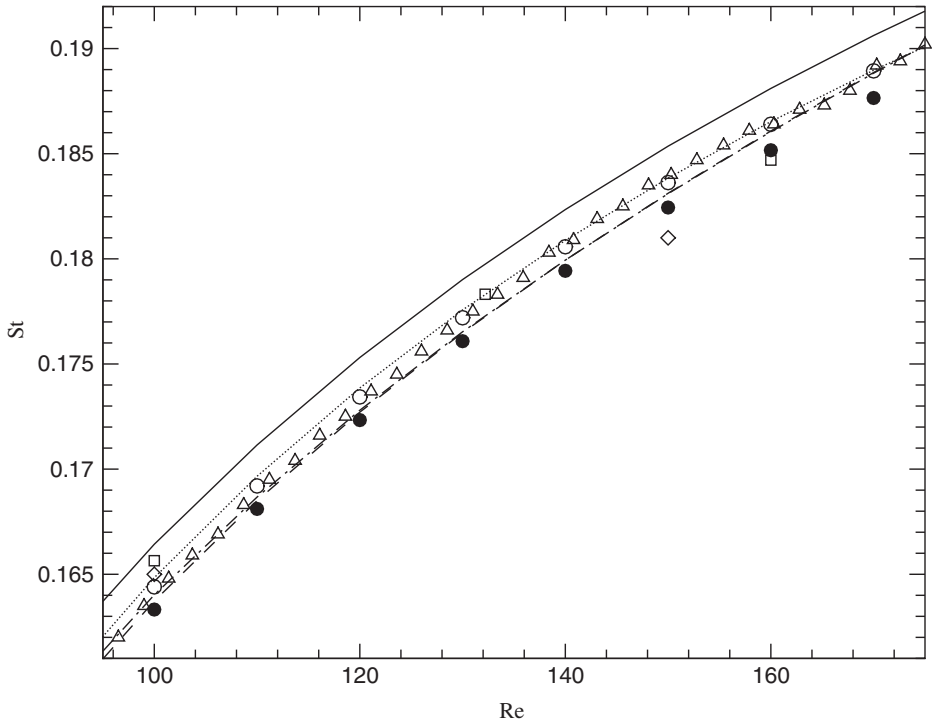

Fig. 14. Strouhal–Reynolds number relationship at $100 \leqslant Re \leqslant 170$: —, Henderson (1997); □, Lange (1997); ◇, Persillon and Braza (1998); ○, present work $L_{b|i} = 70D$; •, present work $L_{b|i} = 4000D$ (all numerics); ·····, Fey (1998); – – – – ––, Leweke and Provansal (1995); – · – · –, Norberg (1994); △, Williamson (1989) (all experiments).

The experimental data that are included in Figs. 13 and 14 are given as polynomial approximations in literature: $St = 0.2684 - 1.0356/\sqrt{Re}$ in Fey (1998), $St = -3.669/Re + 0.1861 + 0.0001432\,Re$ in Leweke and Provansal (1995), and $St = -3.458/Re + 0.1835 + 1.51 \times 10^{-4} Re$ in Norberg (1994). An exception are the results of Williamson (1989) that are included directly. All curves fit together within the accuracy of measurement errors. However, it should be noted that the lower Strouhal numbers have been obtained by using large length-to-diameter ratios (L/D) of the cylinder. Logically Norberg (L/D up to 2000) and Leweke and Provansal (measurements on a ring in order to avoid end-effects) got the lower border of results, as shown in Fig. 14. Nevertheless the measurements and data of the present work are placed very close together. Taking the data of Fey as the upper border and of Leweke and Provansal as the lower border, the error amounts to about 0.7% at most Reynolds numbers. The scatter of experimental results is larger only for $Re < 60$. Note that the experimental curves drop for $Re \approx 180$ because of the transition to three-dimensionality and deviate from two-dimensional numerical results (Posdziech and Grundmann, 2001). Fey (1998) could sustain a two-dimensional cylinder flow up to $Re \approx 230$ by means of two thin wires, tightened parallel to the cylinder axis at $x/D = 1.05$, $\phi = \pm 174^\circ$. His measurements confirm the two-dimensional calculations for $Re > 180$.

The Strouhal–Reynolds number relationship is usually given in the literature in the form of curve-fits. Roshko (1954) used the correlation $St = 0.212 + 4.5/Re$. Later, different authors published similar representations by variation of the coefficients. A detailed summary of definitions and discussion of accuracy can be found in Williamson and Brown (1998). Traditionally, polynomial approximations with two and three terms were used. Later, Williamson (private communication) and Fey (1998) proposed a fit with a square-root expansion $St = a_0 + a_1/\sqrt{Re}$. Fey plotted his data in the form $St(1/\sqrt{Re})$, so a straight line was obtained in the St versus Re dependency. Tests with measurements of Williamson and the present data show consistent deviations from that curve, supporting a more complex law. Williamson and Brown (1998) executed a series expansion in $1/\sqrt{Re}$ and truncated the series after the third term to obtain a three-term St–Re relation.

Following the work of Williamson and Brown, data of the present work are fitted to the traditional and square-root expansions for $50 \leqslant Re \leqslant 250$. Furthermore, a new law is proposed using noninteger polynomials:

$$St = a_0 + a_1 Re^{-a_2}. \tag{12}$$

The present numerical data have negligible variations compared to the scatter in measurements, therefore curve-fits are easier to perform. Table 8 lists the expansions and generated coefficients together with the average error $\bar{\varepsilon}$ and the maximum error ε_{max} as defined in Eq. (8) as well as Eq. (9) and used in Williamson and Brown (1998). The coefficients are determined at a domain size of $L_{b|i} = 70D$, since the results are very smooth here. Compared are polynomials with two and three terms in traditional form, square-root expansions and the usage of noninteger polynomials. The definitions are included in Table 8.

Table 8
Comparison of St versus Re curve-fits for $50 \leqslant Re \leqslant 250$ and $L_{b|i} = 70D$

Curve-fit	Coefficients	$\bar{\varepsilon}$	ε_{max}
2-term traditional $St = a_0 + \frac{a_1}{Re}$	$a_0 = 0.218673$ $a_1 = -4.7961$	2.94×10^{-3}	6.50×10^{-3}
3-term traditional $St = a_0 + \frac{a_1}{Re} + a_2 Re$	$a_0 = 0.189629$ $a_1 = -3.6439$ $a_2 = 1.2 \times 10^{-4}$	4.93×10^{-4}	1.51×10^{-3}
2-term square root $St = a_0 + \frac{a_1}{\sqrt{Re}}$	$a_0 = 0.267892$ $a_1 = -1.0263$	3.83×10^{-4}	8.61×10^{-4}
3-term square root $St = a_0 + \frac{a_1}{\sqrt{Re}} + \frac{a_2}{Re}$	$a_0 = 0.276052$ $a_1 = -1.1965$ $a_2 = 0.79547$	6.25×10^{-5}	4.90×10^{-4}
2-term noninteger polynomial $St = a_0 + a_1 Re^{-a_2}$	$a_0 = 0.284397$ $a_1 = -0.870566$ $a_2 = 0.4304$	5.76×10^{-5}	3.82×10^{-4}

The mean as well as the maximum errors decrease from the top to the bottom of the table. The square-root expansion outmatches the traditional forms, as already shown in Fey (1998) and Williamson and Brown (1998). The addition of a third term by Williamson and Brown again improves the accuracy of the polynomial fit. The two-term noninteger polynomial fits best to data of the present work in the scope concerned. The formulation is rather simple and could therefore be preferred in order to validate numerical as well as experimental results. If the noninteger polynomial is applied to the asymptotic solution at $L_{b|i} = 4000D$, the following equation results:

$$\mathrm{St} = 0.278484 - 0.896502\mathrm{Re}^{-0.445775}. \tag{13}$$

Eq. (13) is valid for $50 \leqslant \mathrm{Re} \leqslant 250$. However, it should be noted that experimental results drop at $\mathrm{Re} \approx 170$–180 because of the development of three-dimensional modes.

7. Conclusions

The flow around an infinitely long circular cylinder, in the center of interest for more than one century, still raises many questions. A large scatter in numerical data was obtained even in the 'simple' two-dimensional, laminar regime. The deviations are mostly caused by a grid dependency of solutions. In the present work a spectral element method was used to show how fundamental quantities like drag, lift, base-pressure coefficient, and Strouhal number can be computed consistently by varying both the resolution and the domain extension so that experimental results are confirmed within the range of measurement errors. Furthermore, the scatter in previous numerical data could be largely assessed.

Different computational domains with extensions from $L_{b|i} = 20D$ up to $L_{b|i} = 4000D$ were used to obtain asymptotic solutions in the steady and unsteady flow regime. Holding the domain size constant, the order of polynomial basis was increased until the solution does not change anymore. It was shown that the domain extension governs the accuracy of numerical results. Studies at different Reynolds numbers in the steady and unsteady flow regime allowed the evaluation of blockage effects in terms of integral quantities of the cylinder flow. The Strouhal number, frequently used for a comparison between numerics and experiments, is less affected by errors introduced by blockage and resolution shortcomings. The flow forces and the base-pressure coefficient turned out to be more stringent criteria for the investigation of grid independence. Most numerical works, that turned out to be inaccurate, used the Strouhal number for the verification of the computational grid. The results are useful for similar investigations in order to estimate the error that has to be taken into account by finite computational domains. For that, the dependency of the flow quantities on the domain extension was given as curve-fit using noninteger polynomials.

Reynolds number relationships of drag and base-pressure coefficients in the steady flow regime and in addition Strouhal number and lift coefficient in the unsteady range were computed at domain extensions of $L_{b|i} = 70D$ and $4000D$. The first domain size represents a compromise between accuracy and expenditure, whereas the latter describes the asymptotic solution. All Reynolds number dependencies are given as polynomial approximations. In the case of the Strouhal number, different representations are discussed and compared to the literature. From the intersection of steady and unsteady Reynolds number relationships, the critical Reynolds number of the primary instability was determined to $\mathrm{Re}_C = 46.7$ in perfect correspondence to experimental and numerical data.

The computation of drag and lift coefficients on bluff bodies like circular cylinders, buildings in environmental fluid mechanics, or even cars requires large computational domains to minimize blockage effects. The present work shows that a very careful validation of the numerical grid, both in terms of resolution and domain size, is necessary to obtain grid-independent solutions. If this is done, a perfect agreement between numerical and experimental data can be obtained, at least in the laminar flow regime.

Acknowledgements

We thank Prof. G.E. Karniadakis (Brown University, Providence, USA) for the donation of the spectral element code. The support of Deutsche Forschungsgemeinschaft (DFG INK 18 B1-1 TP A2) is gratefully acknowledged, and we want to thank the Center for High-Performance Computing of Dresden University of Technology for providing very extensive computational resources.

References

Anagnostopoulos, P., Iliadis, G., Richardson, S., 1996. Numerical study of the blockage effects on viscous flow past circular cylinders. International Journal of Numerical Methods Fluids 22, 1061–1074.

Berger, E., 1964. Die Bestimmung der hydrodynamischen Größen einer Kármánschen Wirbelstraße aus Hitzdrahtmessungen bei kleinen Reynolds Zahlen. Zeitschrift Flugwissenschaften und Weltraumforschung 12, 41–59.

Behr, M., Hastreiter, D., Mittal, S., Tezduyar, T.E., 1995. Incompressible flow past a circular cylinder: dependence of the computed flow field on the location of the lateral boundaries. Computational Methods in Applied Mechanical Engineering 123, 309–316.

Braza, M., Chassaing, P., Minh, Ha, 1986. Numerical study and physical analysis of the pressure and velocity fields in the near wake of a circular cylinder. Journal of Fluid Mechanics 165, 79–130.

Dennis, S.C.R., 1976. A numerical method for calculating steady flow past a cylinder. In: A.I. van de Vooren, P.J. Zandbergen, eds., Proceedings of the Fifth International Conference on Numerical Methods in Fluid Dynamics. Lecture Notes in Physics, vol. 59, Springer, Berlin, pp. 165–171.

Fey, U., 1998. Eine neue Gesetzmäßigkeit für die Wirbelfolgefrequenz des Kreiszylinders und Steuerung der Instabilitäten im Bereich $160 < \mathrm{Re} < 300$. MPI für Strömungsforschung Report 3, Göttingen.

Fornberg, B., 1980. A numerical study of steady viscous flow past a circular cylinder. Journal of Fluid Mechanics 98, 819–855.

Franke, R., Rodi, W., Schönung, B., 1990. Numerical calculation of laminar vortex-shedding flow past cylinders. Journal of Wind Engineering and Industrial Aerodynamics 35, 237–275.

Gerich, D., Eckelmann, H., 1982. The influence of end plates and free ends on the shedding frequency of circular cylinders. Journal of Fluid Mechanics 122, 109–121.

Henderson, R.D., 1995. Details of the drag curve near the onset of vortex shedding. Physics of Fluids 7, 2102–2104.

Henderson, R.D., 1997. Nonlinear dynamics and pattern formation in turbulent wake transition. Journal of Fluid Mechanics 352, 65–112.

Henderson, R.D., Karniadakis, G.E., 1995. Unstructured spectral element methods for simulation of turbulent flows. Journal of Computational Physics 122, 191–217.

Jackson, C.P., 1987. A finite-element study of the onset of vortex shedding in flow past variously shaped bodies. Journal of Fluid Mechanics 182, 23–45.

Karniadakis, G.E., Israeli, M., Orszag, S.A., 1991. High-order splitting methods for the incompressible Navier–Stokes equations. Journal of Computational Physics 97, 415–443.

Kravchenko, A.G., Moin, P., Shariff, K., 1999. B-spline method and zonal grids for simulations of complex turbulent flows. Journal of Computational Physics 151, 757–789.

Lange, C., 1997. Numerical predictions of heat and momentum transfer from a cylinder in crossflow with implications to hot-wire anemometry. Ph.D. Thesis, University Erlangen-Nürnberg.

Leweke, T., Provansal, M., 1995. The flow behind rings: bluff body wakes without end effects. Journal of Fluid Mechanics 288, 265–310.

Norberg, C., 1994. An experimental investigation of the flow around a circular cylinder: influence of aspect ratio. Journal of Fluid Mechanics 258, 287–316.

Park, J., Kwon, K., Choi, H., 1998. Numerical solutions of flow past a circular cylinder at Reynolds numbers up to 160. KSME International Journal 12, 1200–1205.

Persillon, A., Braza, M., 1998. Physical analysis of the transition to turbulence in the wake of a circular cylinder by three-dimensional Navier–Stokes simulation. Journal of Fluid Mechanics 365, 23–88.

Posdziech, O., Grundmann, R., 2001. Numerical simulation of the flow around an infinitely long circular cylinder in the transition regime. Theoretical and Computational Fluid Dynamics 15, 121–141.

Provansal, M., Mathis, C., Boyer, L., 1987. Bénard–von Kármán instability: transient and forced regimes. Journal of Fluid Mechanics 182, 1–22.

Roshko, A., 1954. On the development of turbulent wakes from vortex streets. NACA Report 1191.

Rosenfeld, M., 1994. Grid refinement test of a time periodic flow over bluff bodies. Computers & Fluids 23, 693–709.

Strouhal, V., 1878. Über eine besondere Art der Tonerregung. Annalen Physik und Chemie. Neue Folge 5, 216–251.

Tritton, D.J., 1959. Experiments on the flow past a circular cylinder at low Reynolds numbers. Journal of Fluid Mechanics 6, 547–567.

Wieselsberger, C., 1921. Neuere Feststellungen über die Gesetze des Flüssigkeits- und Luftwiderstands. Physikalische Zeitschrift 22, 321–328.

Williamson, C.H.K., 1989. Oblique and parallel modes of vortex shedding in the wake of a circular cylinder at low Reynolds numbers. Journal of Fluid Mechanics 206, 579–627.

Williamson, C.H.K., 1992. The natural and forced formation of spot-like 'vortex dislocations' in the transition wake. Journal of Fluid Mechanics 206, 579–627.

Williamson, C.H.K., Brown, G.L., 1998. A series in $1/\sqrt{\mathrm{Re}}$ to represent the Strouhal–Reynolds number relationship of the cylinder wake. Journal of Fluids and Structures 12, 1073–1085.

Williamson, C.H.K., Roshko, A., 1990. Measurements of base pressure in the wake of a cylinder at low Reynolds numbers. Zeitschrift Flugwissenschaften und Weltraumforschung 14, 38–46.

Yang, H.H., Seymour, B.R., Shizgal, B.D., 1994. A Chebyshev pseudospectral multi-domain method for steady flow past a cylinder up to $\mathrm{Re} = 150$. Computers & Fluids 23, 829–851.